Nano Research

Open Access

Research Article

Electron-rich Pt active sites enable efficient complete dehydrogenation electrooxidation of formic acid on Pt/Ag@Bi_2Te_3 triple-phase heterointerfaces

Aining Tao[1], Qiang Yuan[1] ✉, Kaiyu Dong[1], Siyang Nie[2,3], and Xun Wang[2] ✉

[1] *State Key Laboratory of Green Pesticide, Centre for R & D of Fine Chemicals, College of Chemistry and Chemical Engineering, Guizhou University, Guiyang 550025, China*
[2] *Department of Chemistry, Tsinghua University, Beijing 100084, China*
[3] *School of Energy and Environment, City University of Hong Kong, Kowloon, Hong Kong, China*

Cite this article: *Nano Research*, **2026**, *19*, 94908677. https://doi.org/10.26599/NR.2026.94908677

ABSTRACT: Realizing the dehydrogenation direct pathway of formic acid electrooxidation reaction (FAOR) via sequential dehydrogenation steps is crucial for direct formic acid proton exchange membrane fuel cells (DFAPEMFCs). Herein, a two-dimensional porous Pt/Ag@Bi_2Te_3 electrocatalyst featuring a triple-phase heterointerface is prepared via a visible light-induced strategy. The heterointerface effect and metal–support effect endow the Pt active sites with local electron-rich properties, thereby facilitating attack on the H atom of H–COO–H to cleave the C–H and O–H bonds and realize the direct pathway. The Pt/Ag@Bi_2Te_3 demonstrates remarkable FAOR mass and specific activities of 10.7 $A \cdot mg_{Pt}^{-1}$ and 45.46 $mA \cdot cm^{-2}$, outperforming commercial Pt/C by factors of 21.8 and 11.4, respectively. In the practical DFAPEMFC device, the Pt/Ag@Bi_2Te_3 delivers a peak power density of 116.2 $mW \cdot cm^{-2}$, indicating its application potential. Density functional theory calculations further confirm the electron-rich Pt active sites and higher energy efficiency for the complete dehydrogenation direct pathway. This study provides a new strategy for preparing highly efficient FAOR catalysts for actual DFAPEMFCs.

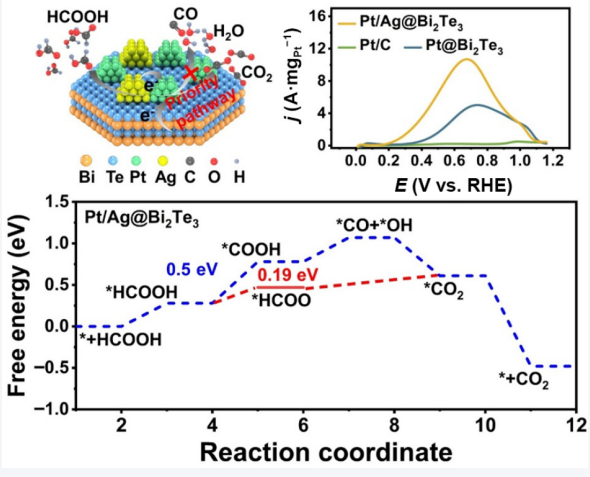

KEYWORDS: Pt-based electrocatalyst, triple-phase heterointerface, formic acid electrooxidation, dehydrogenation direct pathway fuel cells

1 Introduction

The distinct advantages of a high volumetric energy density (formic acid: 1.75 $kWh \cdot L^{-1}$; hydrogen energy: 1.3 $kWh \cdot L^{-1}$) as well as ease of storage and transportation make direct formic acid proton exchange membrane fuel cells (DFAPEMFCs) are considered one of the promising energy conversion devices [1–4]. Moreover, during the anodic formic acid oxidation reaction (FAOR), a single molecule of formic acid yields only one molecule of carbon dioxide (CO_2) that can be electrochemically reduced, which enables a sustainable CO_2 cycle (carbon neutrality as the strategic objective) [5–7]. Generally, FAOR involves the transfer of two electrons and two protons, and scientists typically consider it to follow two reaction mechanisms (Scheme 1): One is the direct pathway via sequential dehydrogenation (HCOOH → *HCOO + H^+ + e^- → CO_2 + 2H^+ + 2e^-) and the other is the indirect pathway via dehydration (HCOOH → *CO + H_2O → CO_2 + 2H^+ + 2e^-) [8–10]. The abundance of continuous Pt active sites on larger Pt-based nanoparticle catalysts facilitates the stable adsorption of the adsorption intermediate (*CO), and thereby slows down the kinetics of the direct pathway for FAOR and facilitates the indirect pathway [11–13]. Furthermore, the *CO generated via the dehydration pathway of FAOR can block the active sites of the electrocatalyst and thereby impede the sustained reaction process.

Received: March 16, 2026; **Revised:** March 21, 2026
Accepted: March 25, 2026

✉Address correspondence to Qiang Yuan, qyuan@gzu.edu.cn; Xun Wang, wangxun@mail.tsinghua.edu.cn

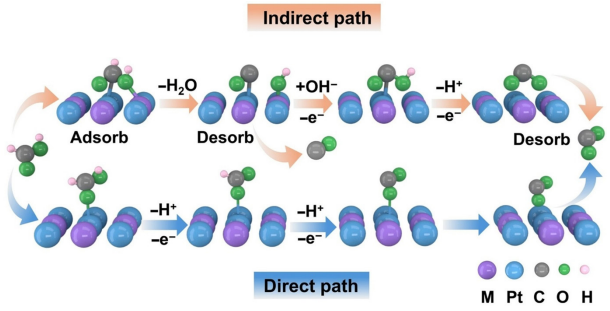

Scheme 1 Mechanism of formic acid electrooxidation.

Consequently, the operational efficiency of DFAPEMFCs is reduced. Therefore, it is of crucial importance to change the FAOR pathway from the indirect route to the direct route of sequential dehydrogenation via the structural design of electrocatalysts, and to accelerate the reaction kinetics of the direct pathway [14–16].

The rational design of electrocatalysts via interface engineering plays a vital role. The interfaces formed by two or more components within heterogeneous electrocatalysts are crucial in the electrocatalytic process [17–19]. In heterostructure electrocatalysts, synergistic effects at the interfaces between different components considerably accelerate reaction kinetics by balancing the adsorption/desorption behavior of the intermediate reaction [20, 21]. Moreover, interface engineering can modulate the electronic structure of active sites via electronic interactions between different components, thereby optimizing the binding energy between active sites and intermediate products [22–24]. For example, the synergistic interaction between the hexagonal close-packed phase and the face-centered cubic phase in the Ru–Sn nanoflower structure modulates the adsorption energy of H, weakens the binding energy of CO, and thereby accelerates the kinetics of the electrooxidation reaction [25]. Moreover, metal-support interactions also play a crucial role in regulating catalyst performance. Specifically, the support modulates of the metal and orbital rehybridization at the interface can effectively adjust the d-band centers of the metal atoms and optimize the intrinsic adsorption–desorption properties of electrocatalysts [26, 27]. Two-dimensional (2D) hexagonal Bi_2Te_3 semiconductor nanomaterials have gained traction owing to their superior electrical conductivity, high specific surface area, and unprecedented optoelectronic properties [28, 29]. However, studies aimed at achieving precise control over electronic structures and electrocatalytic performance using synergistic effects between interface engineering and metal–support interactions remain relatively limited, particularly in the field of advanced Pt-based electrocatalysts designed for FAOR applications.

Herein, we report a Pt/Ag@Bi_2Te_3 electrocatalyst that co-anchors Pt and Ag heteronanoparticles via a visible light–induced strategy, which facilitates the coexistence of triple-phase heterointerfaces and precisely tunes the electronic structure and performance of the primary Pt active sites. Compared with Pt@Bi_2Te_3, the introduction of Ag further adjusts the d-band structure of Pt and thereby changes the local coordination environment to optimize HCOOH adsorption and effectively suppress *CO intermediates formation. The prepared triple-phase heterointerfaces catalyst demonstrates enhanced FAOR performance. Its mass activity (MA) and specific activity (SA) are 21.8 times and 11.4 times higher than those of commercial Pt/C catalysts, respectively. In addition, in practical DFAPEMFCs, the peak power density of Pt/Ag@Bi_2Te_3 reaches 116.2 mW·cm^{-2}. Density functional theory (DFT) further reveals that the introduction of Ag enriches the charge at Pt active sites on the Pt/Ag@Bi_2Te_3 surface and thereby suppresses the intrinsic CO formation and promotes the direct FAOR pathway for complete dehydrogenation.

2 Experimental section

2.1 Materials

Chloroplatinic acid ($H_2PtCl_6·6H_2O$, 99.9%) was purchased from Aldrich. Silver nitrate ($AgNO_3$, AR), bismuth chloride ($BiCl_3$, AR), and tellurium oxide (TeO_2, AR) were purchased from Macklin. Polyvinylpyrrolidone (PVP, P40) was purchased from Aldrich. Sodium hydroxide (NaOH, AR), ethanol (99.8%), ethylene glycol (EG, AR), formic acid (HCOOH, AR), and sulfuric acid (H_2SO_4, 98%, AR) were purchased from Sinopharm Chemical Reagent Co. Ltd. (Shanghai, China). Pt/C (20 wt.% and 60 wt.%) catalyst was obtained from Johnson Matthey. Vulcan XC-72 was got from Cabot. $H_2PtCl_6·6H_2O$ and $AgNO_3$ need to be further diluted with a concentration of 0.01 M.

2.2 Synthesis of Bi_2Te_3 seeds

Bi_2Te_3 nanoplates were synthesized according to a previously reported method [30]. In detail, 0.4 g of PVP, 0.315 g of $BiCl_3$, 0.24 g of TeO_2, and 0.5 g of NaOH were added to 22.5 mL of EG and stirred at room temperature for 60 min in a 45 mL Teflon-lined stainless-steel autoclave. The sealed autoclave was heated at 180 °C for 9 h and cooled to room temperature. The product was washed three times with ethanol at 10,000 rpm for 30 min, and the final product was dispersed in 30 mL of ethanol.

2.3 Synthesis of Pt/Ag@Bi_2Te_3, Pt@Bi_2Te_3, and Ag@Bi_2Te_3

The synthesis was performed via a visible light-assisted template method. Specifically, 0.5 mL solution of Bi_2Te_3 seeds, 0.9 mL 0.01 M chloroplatinic acid, and 0.1 mL 0.01 M $AgNO_3$ were added into a culture dish containing 10 mL of EG. Following stirring for 5 min at room temperature, the culture dish was placed in a dark room and irradiated with a table lamp (tungsten lamp, 40 W) for 2 h. The product was centrifuged two times at 10,000 rpm with ethanol and dispersed in 4 mL of ethanol. The Pt/Bi_2Te_3 and Ag@Bi_2Te_3 were synthesized following the same procedure for synthesis of Pt/Ag@Bi_2Te_3 without using $AgNO_3$ and chloroplatinic acid.

3 Results and discussion

3.1 Structure characterizations of Pt/Ag@Bi_2Te_3

Figure 1(a) presents a schematic diagram of the synthesis process of the heterostructure Pt/Ag@Bi_2Te_3 2D nanoplate via a straightforward solvothermal method combined with the photochemical method. A Bi_2Te_3 hexagonal nanoplate with a thickness of ~ 29.9 nm was prepared using $BiCl_3$ and TeO_2 as metal precursors (Fig. S1(a) in the Electronic Supplementary Material (ESM)). Subsequently, photogenerated electrons were generated using Bi_2Te_3 as a template under visible light and successfully reduced Pt^{4+} and Ag^+ heterogeneous nanoparticles. The nanoparticles were anchored on the template surface to form a triple-phase symbiotic heterogeneous structure composed of Pt, Ag, and Bi_2Te_3. Transmission electron microscopy (TEM) and high-

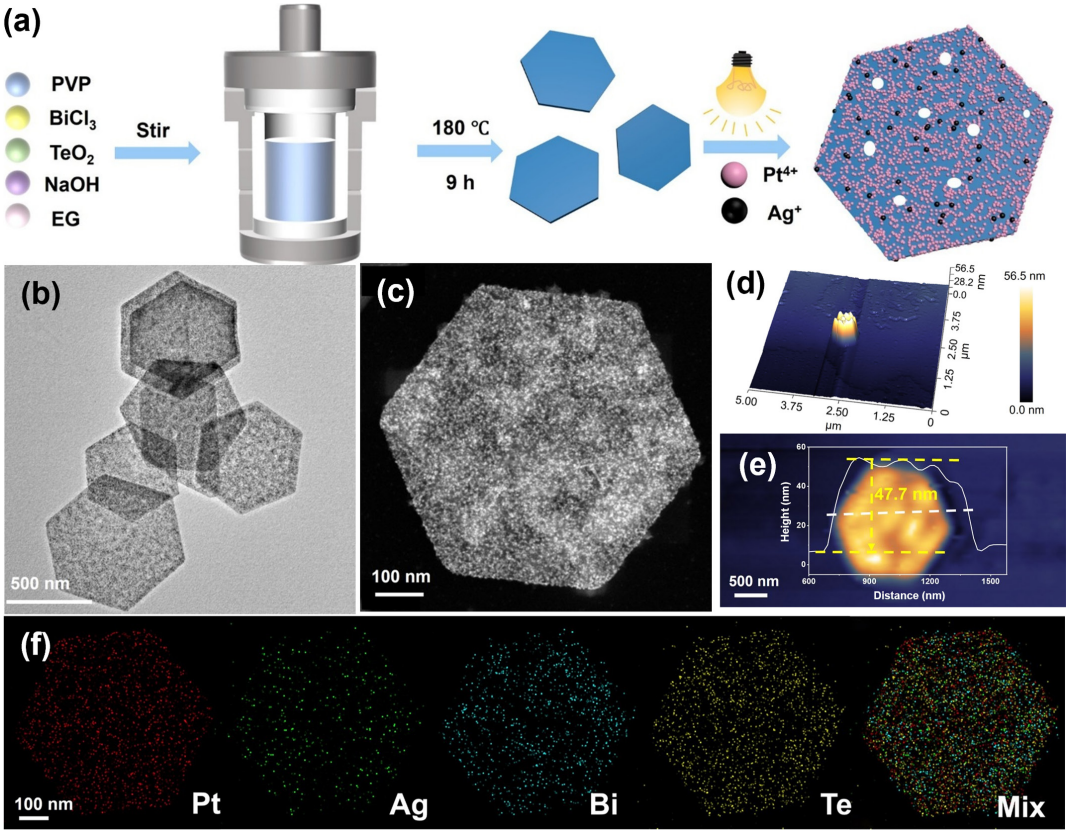

Figure 1 Synthesis and structure characterizations of Pt/Ag@Bi_2Te_3. (a) Schematic illustrating the synthesis of Pt/Ag@Bi_2Te_3. (b) TEM image, (c) HAADF-STEM image, (d) and (e) AFM images and the corresponding height profiles, and (f) corresponding elemental mapping images of Pt/Ag@Bi_2Te_3.

angle annular dark-field scanning transmission electron microscopy (HAADF-STEM) images reveal that Pt and Ag nanoparticles are uniformly anchored onto the surface of Bi_2Te_3 nanoplates (Figs. 1(b) and 1(c)). The three-dimensional (3D) atomic force microscopy (AFM) image shows the rough and uneven surface of Pt/Ag@Bi_2Te_3, which is further confirmed by the 2D AFM image, with a maximum thickness of ~ 47.7 nm (Figs. 1(d) and 1(e), and Fig. S1(b) in the ESM). Owing to the leaching of Bi and Te elements during irradiation, porous structures were form (Fig. S2 in the ESM), which facilitate mass transport and thereby enhance the electrocatalytic reaction performance [31–33]. The elemental mapping in (Fig. 1(e)) indicates that this heterostructure comprises four elements: Pt, Ag, Bi, and Te. Inductively coupled plasma optical emission spectroscopy (ICP-OES) measurements indicate that Pt and Ag contents in Pt/Ag@Bi_2Te_3 are 45.8% and 4.7%, respectively (Table S1 in the ESM).

X-ray diffraction (XRD) patterns exhibit two sets of diffraction peaks for Pt@Bi_2Te_3 without Ag, while Pt/Ag@Bi_2Te_3 exhibits three distinct sets of diffraction peaks (Fig. 2(a)). The diffraction peaks at 39.9°, 46.8°, 67.9°, and 81.6° correspond to the (111), (200), (220), and (311) planes of face-centered cubic (fcc) Pt, are referenced in the standard PDF #01-1194, respectively. The diffraction peaks at 37.9° and 44.6° correspond to the (111) and (200) crystal planes of fcc-structured Ag, according to the standard PDF #03-0921. Compared with the standard diffraction peaks of Pt and Ag, these diffraction peaks do not shift, which indicates that Pt and Ag have not formed the alloy phase. The diffraction peaks at 26.3°, 27.7°, 33.4°, 54.2°, 59.0°, 62.36°, and 66.07° correspond attributable to the (104), (015), (018), (0018), (0210), (1115), and (0210) facets of the hexagonal close-packed (hcp) structure Bi_2Te_3, respectively. Moreover, owing to the leaching of Bi and Te elements during visible light irradiation progress, new Bi_2Te_3 diffraction peaks are exposed in Pt/Ag@Bi_2Te_3. XRD results confirm the formation of the three-phase heterointerface in Pt/Ag@Bi_2Te_3. The average particle size of nanoparticles on Pt/Ag@Bi_2Te_3 is ~ 4.11 nm (Fig. 2(b)). HAADF-STEM images (Fig. 2(c)) display abundant interfaces on the Pt/Ag@Bi_2Te_3 particles. The Pt/Ag@Bi_2Te_3 surface exhibits three distinct lattice spacings: 0.226 nm corresponding to the Pt (111) facet, 0.236 nm attributed to the Ag (111) lattice plane, and 0.203 nm corresponding to the Bi_2Te_3 (0015) crystal plane (Figs. 2(d)–2(h)), which is consistent with the aforementioned XRD results. Figures 2(d)–2(f) show the existence of the triple-phase interfaces between Pt, Ag, and Bi_2Te_3. Corresponding fast Fourier transform (FFT) images corroborate the formation of the triple-phase heterointerface, which is consistent with the abovementioned XRD results. Moreover, abundant Pt–Pt homojunction interfaces exist on the Pt/Ag@Bi_2Te_3 surface (Figs. 2(g) and 2(h)). The presence of these abundant interfaces provides abundant active site regions and promotes intense electron transfer that optimizes the adsorption energy of reactants and enhances the electrocatalytic performance [34, 35]. The control sample of Pt@Bi_2Te_3, with a structure similar to that of Pt/Ag@Bi_2Te_3 was synthesized without adding $AgNO_3$ (Fig. S3 in the ESM).

High-resolution X-ray photoelectron spectroscopy (XPS) is employed to further analyze the electronic structural changes in the catalysts. Figure 3(a) illustrates the Pt 4f spectra of commercial Pt/C, Pt@Bi_2Te_3, and Pt/Ag@Bi_2Te_3. Pt simultaneously exhibits metallic and oxidized states, with binding energies of 71.36 and 74.81 eV, which are attributed to the $4f_{7/2}$ and $4f_{5/2}$ electron orbitals of Pt^0, respectively. The binding energies of 72.28 and 75.76 eV

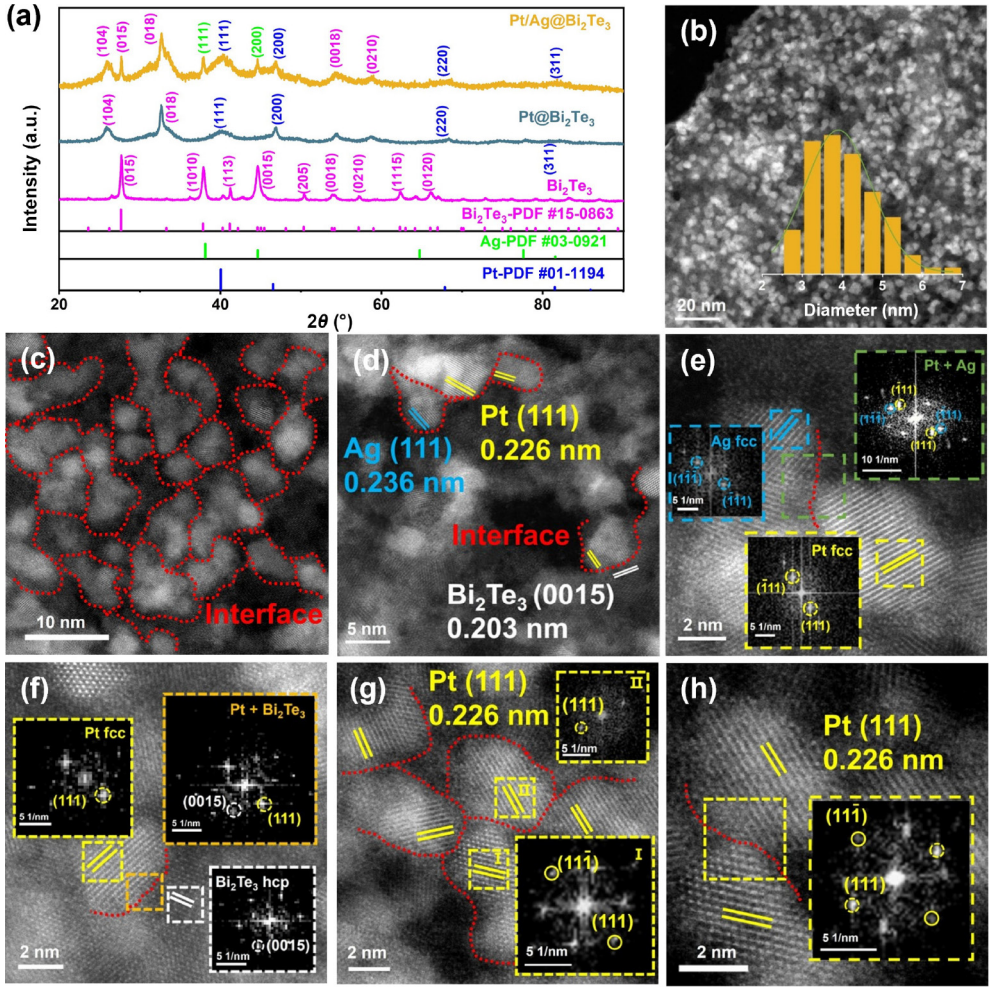

Figure 2 Structure characterizations of Pt/Ag@Bi_2Te_3. (a) XRD patterns of Pt@Bi_2Te_3, Pt/Ag@Bi_2Te_3, and Bi_2Te_3. (b)–(h) The HAADF-STEM images of Pt/Ag@Bi_2Te_3 (the red dashed lines represent interfaces and the corresponding FFT patterns).

correspond to the $4f_{7/2}$ and $4f_{5/2}$ orbitals of Pt^{2+}, respectively. Compared with commercial Pt/C, the binding energies of Pt 4f in Pt@Bi_2Te_3 and Pt/Ag@Bi_2Te_3 exhibit negative shifts of 0.31 and 0.36 eV, respectively. This indicates the presence of strong electron interactions between Pt and other metal atoms, which facilitates optimization of the Pt 4f electronic structure. The binding energy of Ag $3d_{5/2}$ in Pt/Ag@Bi_2Te_3 exhibits a positive shift when compared with standard Ag (Fig. S4(a) in the ESM) [36, 37], which is likely attributed to the lower electronegativity of Ag (1.93) relative to Pt (2.28). Ag is an electron donor, which transfers electrons to Pt and thereby increases the electron density of Pt while reducing its binding energy. The positive shift of Bi 4f and Te 3d binding energies indicates a strong metal–support interaction between Pt and the support (Figs. S4(b) and S4(c) in the ESM). In Pt/Ag@Bi_2Te_3, the positive shift of the Bi 4f binding energy is weaker than that in Pt@Bi_2Te_3, proving that the introduction of Ag alleviates the electron donation pressure of Bi_2Te_3. The shift in the XPS valence band spectra (Fig. 3(b)) equally indicates that the synergistic interaction between the interface and the support causes the d-band center of Pt in Pt/Ag@Bi_2Te_3 to shift upward toward a position closer to the Fermi level [38, 39]. This can optimize the adsorption capacity of the active Pt sites for HCOOH and enhance proton binding and the subsequent dehydrogenation process [40]. The electronic and coordination structures of Pt atoms in Pt@Bi_2Te_3 and Pt/Ag@Bi_2Te_3 are further characterized using X-ray near-edge absorption spectroscopy (XANES) and extended X-ray absorption fine structure (EXAFS). The XANES spectrum reveals that the white line intensity is slightly higher than that of Pt foil but markedly lower than that of PtO_2; this confirms that the Pt species in Pt/Ag@Bi_2Te_3 and Pt@Bi_2Te_3 primarily exist in the metallic state (Fig. 3(c)). The EXAFS spectra of Pt@Bi_2Te_3 and Pt/Ag@Bi_2Te_3 show scattering peaks at 2.76 and 2.75 Å, respectively, which can be attributed to Pt–Pt bonds (Figs. 3(d)–3(f) and Fig. S5 in the ESM). In addition, the coordination numbers of the Pt–Pt bond and Pt–Ag/Bi/Te bonds in Pt/Ag@Bi_2Te_3 are 10.8 and 0.9, respectively (Table S2 in the ESM), approaching the results for Pt@Bi_2Te_3. This confirms the presence of metallic Pt nanoparticles and the existence of metal–support interactions. Wavelet analysis (WT) of the Pt L_3 edge EXAFS for Pt/Ag@Bi_2Te_3 and Pt@Bi_2Te_3 indicates the presence of alloy bonds and metallic bonds, which further validates the bonding structure of the catalysts (Figs. 3(g)–3(i)). The abovementioned results conclusively demonstrate that Pt/Ag@Bi_2Te_3 is not a simple physical mixture. Instead, it achieves synergistic effects between the interface and the support via the formation of a three-phase heterointerface, thereby optimizing the surface charge distribution of the catalyst and considerably enhancing its electrocatalytic performance [41].

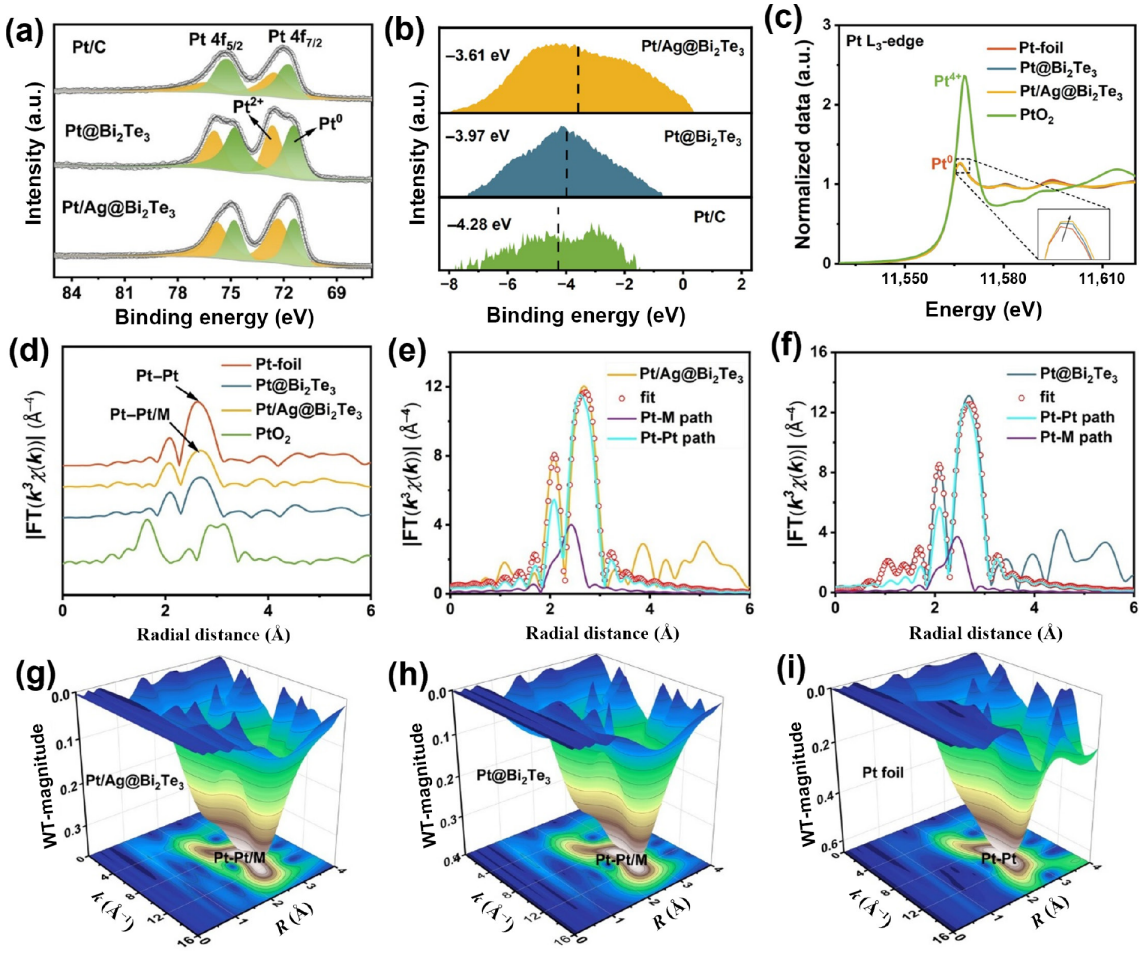

Figure 3 XPS, XANES, and EXAFS. (a) XPS spectra of Pt 4f. (b) XPS valence-band spectra. (c) Pt L_3-edge XANES spectra. (d) FT-EXAFS spectra. Pt L_3-edge EXAFS fitting of (e) $Pt/Ag@Bi_2Te_3$ and (f) $Pt@Bi_2Te_3$. WTs of EXAFS spectra for (g) $Pt/Ag@Bi_2Te_3$, (h) $Pt@Bi_2Te_3$, and (i) Pt foil.

3.2 FAOR and performances of $Pt/Ag@Bi_2Te_3$

The FAOR performances of commercial Pt/C, $Pt@Bi_2Te_3$, and $Pt/Ag@Bi_2Te_3$ are evaluated under acidic conditions. Figure S6 in the ESM exhibited the CV curves of all electrocatalysts recorded in a N_2-saturated 0.5 M H_2SO_4 solution. The electrochemical surface areas (ECSA) of commercial Pt/C, $Pt@Bi_2Te_3$, and $Pt/Ag@Bi_2Te_3$ were determined based on the desorption peaks of Cu_{upd}, with the values of 12.37, 18.25, and 23.5 $m^2 \cdot g_{Pt}^{-1}$, respectively (Figs. S7(a)–S7(d) in the ESM). Among these, $Pt/Ag@Bi_2Te_3$ exhibit the highest ECSA value, indicating that $Pt/Ag@Bi_2Te_3$ possesses additional active sites. The FAOR performances of several catalysts are further evaluated in 0.5 M H_2SO_4 + 3 M HCOOH (Figs. 4(a) and 4(b), and Fig. S7(e) in the ESM). When compared with $Pt/Ag@Bi_2Te_3$ and $Pt@Bi_2Te_3$, the cyclic voltammetry (CV) curve of commercial Pt/C exhibits two distinct oxidation peaks, revealing the existence of both direct and indirect paths [42, 43]. In Fig. 4(a) show that the oxidation peak of $Pt/Ag@Bi_2Te_3$ appears at 0.672 V, which is negatively shifted by 61 and 335 mV compared to $Pt@Bi_2Te_3$ and commercial Pt/C, respectively. $Pt/Ag@Bi_2Te_3$ exhibits the highest MA and SA of 10.7 $A \cdot mg_{Pt}^{-1}$ and 45.46 $mA \cdot cm^{-2}$, respectively. These values were 21.8/11.4 and 2.1/1.7 times higher than those of commercial Pt/C and $Pt@Bi_2Te_3$, respectively. Furthermore, $Ag@Bi_2Te_3$ and Bi_2Te_3 show no catalytic activity toward FAOR (Fig. S8 in the ESM), which confirms that the active site for FAOR originates from Pt. $Pt/Ag@Bi_2Te_3$ exhibited the lowest Tafel slope (Fig. 4(c)), indicating that it has faster reaction kinetics during the FAOR process [44–46]. The MA of $Pt/Ag@Bi_2Te_3$ is also superior to most reported Pt-based catalysts for FAOR (Fig. 4(d) and Table S3 in the ESM).

The current density of $Pt/Ag@Bi_2Te_3$ remains higher than that of commercial Pt/C and $Pt/Ag@Bi_2Te_3$ throughout the 3600 s stability test at an operating voltage of 0.4 V vs. RHE (Fig. 4(e)). Furthermore, following a 3 h stability test, the MA of $Pt/Ag@Bi_2Te_3$ remains 23.3 times higher than that of commercial Pt/C (Fig. 4(f)), demonstrating its outstanding FAOR stability. Following stability testing, the particles on the $Pt/Ag@Bi_2Te_3$ did not show significant aggregation, and their average particle size was 4.33 nm. $Pt/Ag@Bi_2Te_3$ maintains the 2D hexagonal nanoplate morphology with anchored nanoparticles while preserving the triple-phase coexisting heterostructure, which better demonstrates its excellent structural and compositional stability (Fig. S9 in the ESM). *In situ* CO antipoisoning tests reveals that the MA of $Pt/Ag@Bi_2Te_3$ decreases by only 22.37%, which is considerably lower than that of Pt/C and $Pt@Bi_2Te_3$, confirming the introduction of Ag further enhancement CO tolerance of $Pt/Ag@Bi_2Te_3$ (Figs. 4(g) and 4(h), and Fig. S10 in the ESM) by tuning the electronic structure of Pt [47–49].

3.3 Mechanism investigation and DFAPEMFCs performance

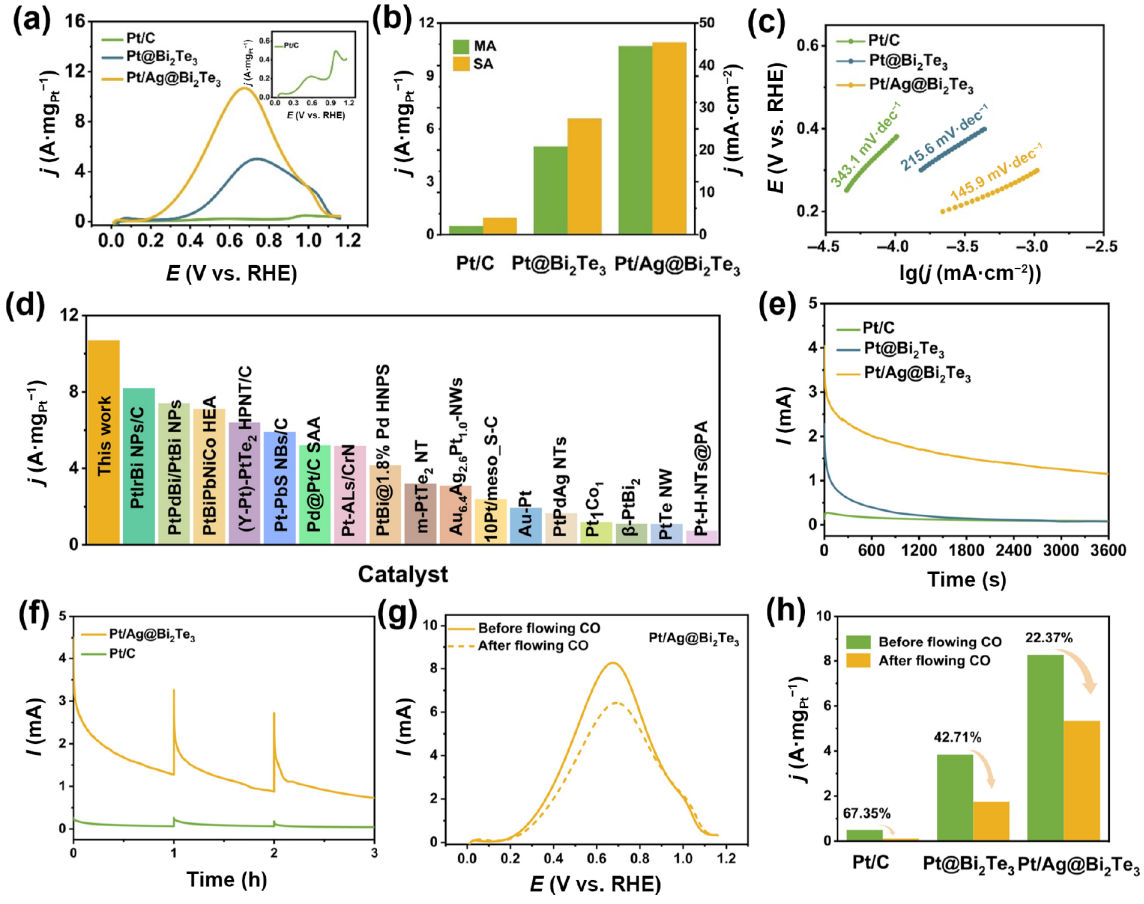

Figure 4 FAOR performance evaluation of $Pt/Ag@Bi_2Te_3$ and other counterparts. (a) Forward-scan CV curves of different catalysts in 0.5 M H_2SO_4 + 3 M HCOOH at a scan rate of 50 mV·s^{-1}. (b) MA and SA of different catalysts for FAOR. (c) Tafel plots of different catalysts. (d) FAOR MA comparison of $Pt/Ag@Bi_2Te_3$ and other reported Pt-based catalysts. (e) Current–time test of commercial Pt/C and different catalysts in 0.5 M H_2SO_4 + 3 M HCOOH. (f) Current–time test curves of $Pt/Ag@Bi_2Te_3$ and commercial Pt/C. (g) *In situ* CO test experiment. (h) Normalized MA before and after flowing CO gas into the electrolyte.

In situ attenuated total reflection surface-enhanced infrared absorption spectroscopy (ATR-SEIRAS) is performed on $Pt/Ag@Bi_2Te_3$, $Pt@Bi_2Te_3$, and commercial Pt/C to further elucidate the mechanism and reaction pathways of FAOR. As shown in Figs. 5(a)–5(c), an *HCOO signal detected at 1730 cm^{-1} indicates that the reaction proceeds via the formate pathway. The signal at 1650 cm^{-1} is attributed to water formation. The banded signal at ~ 2350 cm^{-1} originates from the stretching vibration of CO_2 produced by formic acid oxidation. Meanwhile, the banded signal at ~ 2050 cm^{-1} indicates the formation of *CO [50–52]. During formic acid oxidation, $Pt@Bi_2Te_3$ exhibits weaker CO_L signals than commercial Pt/C, while no *CO is detected on $Pt/Ag@Bi_2Te_3$ (Figs. 5(d)–5(f)). Furthermore, *in situ* real-time spectroscopy (Fig. S11 in the ESM) reveals the emission of CO_2 stretching vibration signals at low potentials, with signal intensity exhibiting a positive correlation with the oxidation potential. The CO_2 signal intensity of $Pt/Ag@Bi_2Te_3$ is considerably higher than that of $Pt@Bi_2Te_3$ and commercial Pt/C catalysts, which comprehensively demonstrates that the triple-phase heterostructure $Pt/Ag@Bi_2Te_3$, which is characterized by interfacial effects, porous structure, and strong charge interactions, exhibits faster FAOR kinetics. The abovementioned analysis indicates that $Pt/Ag@Bi_2Te_3$ not only accomplished formic acid oxidation in acidic media but also achieved a 2e$^-$ complete dehydrogenation pathway (HCOOH → *HCOO + H^+ + e^- → CO_2 + 2e^- + 2H^+), thereby avoiding the adsorption of toxic intermediate products (Fig. 5(g)) [53–55]. This is partly attributed to the synergistic effect between the triple-phase heterogeneous interface and the support regulates the bonding selectivity of Pt atoms toward formic acid oxidation intermediates. Moreover, The introducement of Ag further enhances the ability of Pt to bind protons while suppressing the formation and adsorption of *CO [56, 57], thereby enabling the continuous electrooxidation process of formic acid dehydrogenation.

Compared with the three-electrode system, testing using a practical fuel cell better represents industrial applications [58, 59]. Therefore, we use $Pt/Ag@Bi_2Te_3$ as the anode catalyst in an actual DFAPEMFC device and evaluated its power density. As shown in Fig. 5(h), $Pt/Ag@Bi_2Te_3$ achieves a peak power density of 116.2 mW·cm^{-2} at a current density of 335 mA·cm^{-2}, which is 2.27 times higher than that of commercial Pt/C (51.1 mW·cm^{-2} at 118 mA·cm^{-2}). The DFAPEMFC performance of $Pt/Ag@Bi_2Te_3$ is close to that of the reported catalysts (Table S4 in the ESM). This suggests that $Pt/Ag@Bi_2Te_3$ is a strong candidate for being the anode electrocatalyst in practical DFAPEMFCs.

3.4 DFT calculations

To gain insights into the mechanism of $Pt/Ag@Bi_2Te_3$ triple-phase heterostructures in FAOR, we investigate their reaction thermodynamics in both direct and indirect pathways by performing DFT calculations (Fig. 6). The model of the Pt (111), $Pt@Bi_2Te_3$, and $Pt/Ag@Bi_2Te_3$ in shown in Fig. S12 in the ESM.

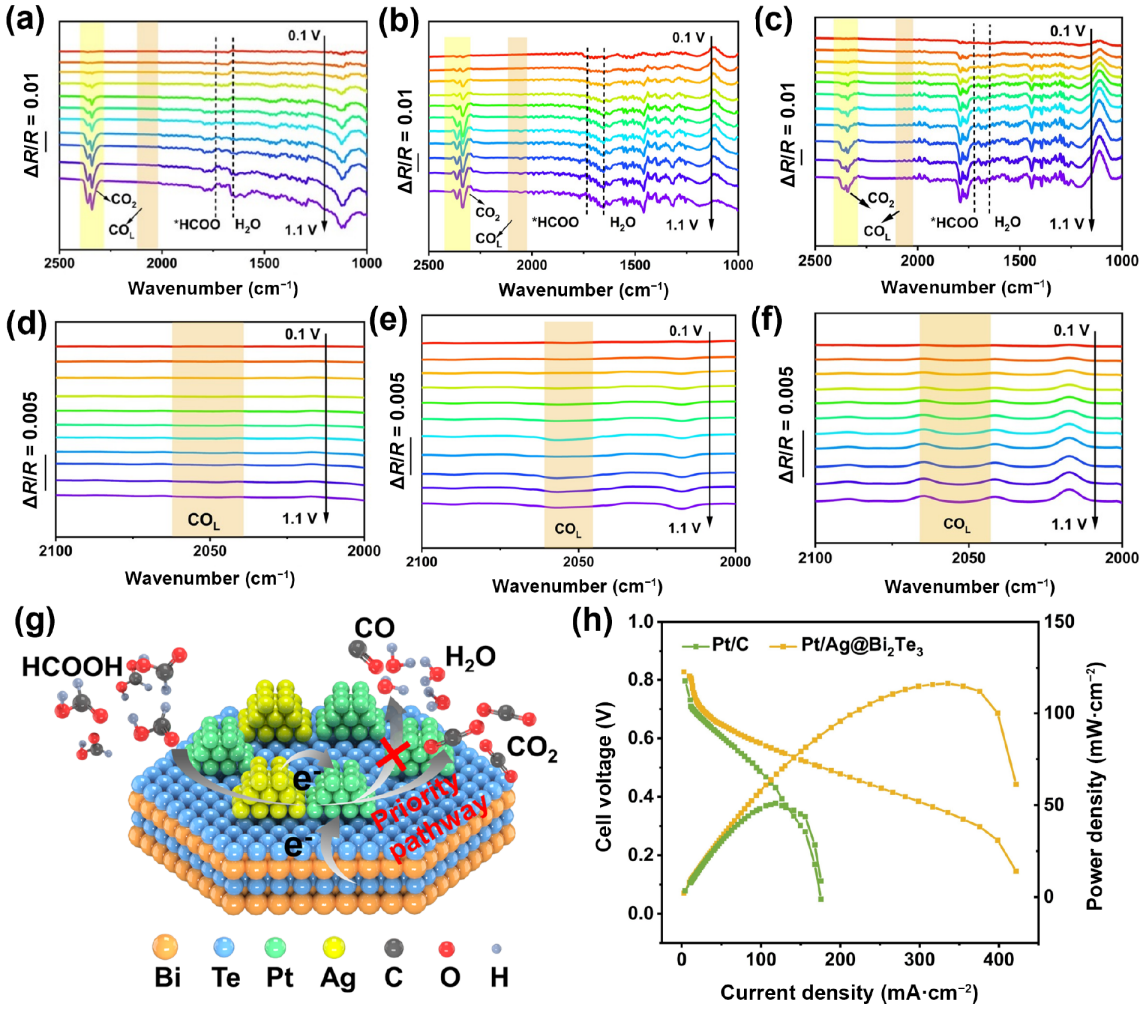

Figure 5 *In situ* ATR-SEIRAS with the potential ranging from 0.1 to 1.1 V vs. RHE of ((a) and (d)) Pt/Ag@Bi_2Te_3, ((b) and (e)) Pt@Bi_2Te_3, and ((c) and (f)) commercial Pt/C. (g) Schematic of the FAOR process of Pt/Ag@Bi_2Te_3. (h) Polarization plots of Pt/Ag@Bi_2Te_3 and commercial Pt/C.

Compared with Pt (111) and Pt@Bi_2Te_3, the total density of states near the Fermi level is enhanced on Pt/Ag@Bi_2Te_3 (Fig. S13 in the ESM), which enables the active site Pt to provide additional electrons and facilitate the activation and subsequent dehydrogenation of HCOOH. The projected partial density of states (PDOS) of Pt@Bi_2Te_3 reveals excellent energy alignment between the Pt 5d orbital and the Bi 6p and Te 5p orbitals (Fig. 6(a)), indicating p–d hybridization between Pt and the support [60]. Pt/Ag@Bi_2Te_3 demonstrates a similar trend (Fig. 6(b)). Furthermore, the Ag 4d orbital and Pt 5d band considerably overlap, indicating strong d–d orbital hybridization between Ag and Pt. Bader charge analysis (Fig. 6(c)) confirms that apart from the carrier transferring electrons to Pt, Ag becomes an electron donor, which supplies electrons to the Pt active sites on the Pt/Ag@Bi_2Te_3 surface, which is consistent with the XPS analysis. This property promotes the binding of Pt with protons in formic acid, thereby enabling complete dehydrogenation during the electrooxidation of formic acid [16]. FAOR generally follows the direct pathway of sequential dehydrogenation (*HCOOH → *HCOO → CO_2) and the indirect pathway of dehydration (*HCOOH → *COOH → *CO → CO_2). Figure 6(d) and Figs. S14 and S15 in the ESM illustrate the adsorption models for Pt (111), Pt@Bi_2Te_3, and Pt/Ag@Bi_2Te_3 in direct and indirect pathways, respectively. Compared with Pt (111) and Pt@Bi_2Te_3, the direct pathway for Pt/Ag@Bi_2Te_3 does not encounter a considerable energy barrier (Figs. 6(e)–6(g)), indicating the more convenient nature of the reaction. The energy barrier difference of the rate-determining step (RDS) between the direct and indirect pathways for Pt/Ag@Bi_2Te_3 is more pronounced than that observed for Pt (111) and Pt@Bi_2Te_3. This indicates that Pt/Ag@Bi_2Te_3 can effectively suppress CO formation and thereby enable the direct pathway to dominate [61]. The RDS energy barriers for both direct and indirect pathways on Pt (111) and Pt@Bi_2Te_3 are relatively close, indicating that both pathways can readily occur on their surfaces which is also consistent with *in situ* ATR-SEIRAS results. In addition, compared with Pt (111) and Pt@Bi_2Te_3, the C–H bond cleavage energy barrier for Pt/Ag@Bi_2Te_3 in the direct pathway is dramatically decreased. Experiments and DFT calculations collectively confirm that the synergistic effect between the Ag-introduced triple-phase heterointerface and the support promotes electron enrichment at Pt sites. This facilitates the attack of Pt active sites on protons of HCOOH, effectively suppressing the formation of intrinsic CO and boosting the direct FAOR pathway for complete dehydrogenation.

4 Conclusions

In summary, 2D Pt/Ag@Bi_2Te_3 hybrid featuring a porous structure

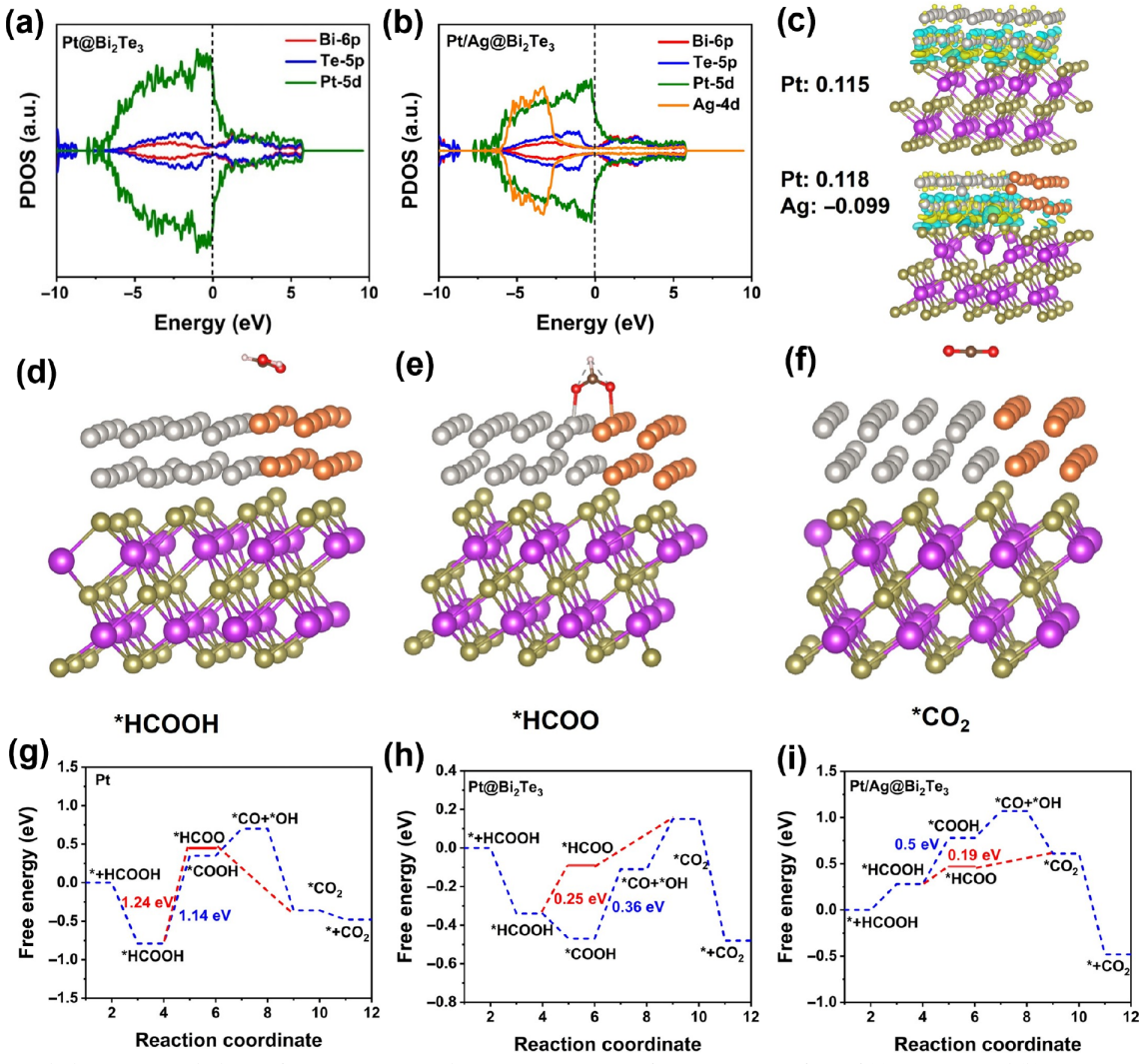

Figure 6 DFT calculations. DFT calculations for Pt, Pt@Bi_2Te_3, and Pt/Ag@Bi_2Te_3. PDOS of *HCOOH on surfaces of (a) Pt@Bi_2Te_3 and (b) Pt/Ag@Bi_2Te_3. (c) Bader charge on the surfaces of Pt@Bi_2Te_3 and Pt/Ag@Bi_2Te_3. (d)–(f) Optimized intermediate structures on Pt/Ag@Bi_2Te_3. gray: Pt, orange: Ag, purple: Bi, yellow: Te, brown: C, red: O, and pink: H. Free energy diagram of (g) Pt, (h) Pt@Bi_2Te_3, and (i) Pt/Ag@Bi_2Te_3 for FAOR.

and a triple-phase heterointerface was successfully prepared via a visible light-induced strategy. Pt/Ag@Bi_2Te_3 demonstrated considerably enhanced activity and stability for FAOR with intrinsic CO resistance, achieving MA of 21.8 and 2.1 times higher than those of commercial Pt/C and a comparable sample of Pt@Bi_2Te_3. In practical DFAPEMFC tests, the Pt/Ag@Bi_2Te_3 achieved a peak power density far more than that of commercial Pt/C. The complete dehydrogenation direct pathway was revealed by *in situ* ATR-SEIRAS. The heterointerface effect and metal–support effect in Pt/Ag@Bi_2Te_3 hybrid were conformed by XPS and EXAFS. DFT calculations further revealed electron enrichment at Pt sites and energy-favorable direct pathway of FAOR over Pt/Ag@Bi_2Te_3. This study provided a novel strategy for the development of highly efficient anode catalysts that would be suitable for DFAPEMFCs and provided insights into the FAOR mechanism via the complete dehydrogenation direct pathway.

Electronic Supplementary Material: Supplementary material (characterization, additional data, and kinetic modeling code) is available in the online version of this article at https://doi.org/10.26599/NR.2026.94907061.

Acknowledgements

This work was supported by the National Natural Science Foundation of China (Nos. 22465009, 22241502, and 22035004) and Education of Department of Guizhou Province (No. 2021312).

Declaration of competing interest

All the contributing authors report no conflict of interests in this work. Author Xun Wang is the Associate Editor of this journal, but he is not involved in the peer-review or decision of this article.

Author contribution statement

A. N. T.: Writing manuscript, validation, methodology, investigation, data curation. Q. Y.: Writing manuscript, validation, supervision, project administration, experimental design, methodology, funding acquisition, formal analysis, data curation, conceptualization. K. Y. D.: Validation, formal analysis, data curation. S. Y. N.: Formal analysis, data curation. X. W.: Project

administration, conceptualization, funding acquisition. All the authors have approved the final manuscript.

Use of AI statement

None.

References

[1] Debe, M. K. Electrocatalyst approaches and challenges for automotive fuel cells. *Nature* **2012**, *486*, 43–51.

[2] Aricò, A. S.; Bruce, P.; Scrosati, B.; Tarascon, J. M.; van Schalkwijk, W. Nanostructured materials for advanced energy conversion and storage devices. *Nat. Mater.* **2005**, *4*, 366–377.

[3] Zhan, C. H.; Bu, L. Z.; Sun, H. R.; Huang, X. W.; Zhu, Z. P.; Yang, T.; Ma, H. B.; Li, L. G.; Wang, Y. C.; Geng, H. B. et al. Medium/high-entropy amalgamated core/shell nanoplate achieves efficient formic acid catalysis for direct formic acid fuel cell. *Angew. Chem., Int. Ed.* **2023**, *62*, e202213783.

[4] Sordakis, K.; Tang, C. H.; Vogt, L. K.; Junge, H.; Dyson, P. J.; Beller, M.; Laurenczy, G. Homogeneous catalysis for sustainable hydrogen storage in formic acid and alcohols. *Chem. Rev.* **2018**, *118*, 372–433.

[5] Xu, P. Z.; Zhang, Z. Q.; Han, L. L. Atomically dispersed catalysts for formic acid oxidation reaction. *J. Energy Chem.* **2025**, *111*, 599–616.

[6] Li, Y.; Yao, M. S.; He, Y. P.; Du, S. F. Recent advances of electrocatalysts and electrodes for direct formic acid fuel cells: From nano to meter scale challenges. *Nano-Micro Lett.* **2025**, *17*, 148.

[7] Firet, N. J.; Smith, W. A. Probing the reaction mechanism of CO_2 electroreduction over Ag films via operando infrared spectroscopy. *ACS Catal.* **2017**, *7*, 606–612.

[8] Chen, X. T.; Granda-Marulanda, L. P.; McCrum, I. T.; Koper, M. T. M. How palladium inhibits CO poisoning during electrocatalytic formic acid oxidation and carbon dioxide reduction. *Nat. Commun.* **2022**, *13*, 38.

[9] Luo, S. P.; Chen, W.; Cheng, Y.; Song, X.; Wu, Q. L.; Li, L. X.; Wu, X. T.; Wu, T. H.; Li, M. R.; Yang, Q. et al. Trimetallic synergy in intermetallic PtSnBi nanoplates boosts formic acid oxidation. *Adv. Mater.* **2019**, *31*, 1903683.

[10] Lee, C. W.; Jung, S. Y.; Ryu, J. H.; Jeon, G. S.; Gaur, A.; Cho, M. S.; Ali, G.; Kim, M.; Chung, K. Y.; Nayak, A. K. et al. Empowering tri-functional palladium's catalytic activity and durability in electrocatalytic formic acid oxidation reaction via innovative self-caging and alloying strategies. *Adv. Sci.* **2024**, *11*, 2405725.

[11] Dong, C. Y.; Zhang, B.; Song, H. J.; Zhou, S. Y.; Ye, J. Y.; Liao, H. G.; Dong, L. S.; Huang, X. Q.; Bu, L. Z. Platinum-tellurium heterojunction nanosheet assemblies for efficient direct formic acid electrooxidation catalysis. *ACS Nano* **2024**, *18*, 10008–10018.

[12] Feng, R. X.; Li, D.; Yang, H. Z.; Li, C. Y.; Zhao, Y. X.; Waterhouse, G. I. N.; Shang, L.; Zhang, T. R. Epitaxial ultrathin Pt atomic layers on CrN nanoparticle catalysts. *Adv. Mater.* **2024**, *36*, 2309251.

[13] Yang, X. L.; Meng, Q. L.; Wang, X.; Jin, Z.; Liu, C. P.; Ge, J. J.; Xing, W. A new pathway for formic acid electro-oxidation: The electro-chemically decomposed hydrogen as a reaction intermediate. *J. Energy Chem.* **2022**, *71*, 188–191.

[14] Osawa, M.; Komatsu, K. I.; Samjeské, G.; Uchida, T.; Ikeshoji, T.; Cuesta, A.; Gutiérrez, C. The role of bridge-bonded adsorbed formate in the electrocatalytic oxidation of formic acid on platinum. *Angew. Chem., Int. Ed.* **2011**, *50*, 1159–1163.

[15] Ferre-Vilaplana, A.; Perales-Rondón, J. V.; Buso-Rogero, C.; Feliu, J. M.; Herrero, E. Formic acid oxidation on platinum electrodes: A detailed mechanism supported by experiments and calculations on well-defined surfaces. *J. Mater. Chem. A* **2017**, *5*, 21773–21784.

[16] Zheng, Z. K.; Liu, B.; Qiu, J. X.; Xu, S. J.; Wang, Y. C.; Zhang, M.; Li, K.; Sun, Z. T.; Li, Z. A.; Wan, Y. Y. et al. Effectively regulating electrooxidation of formic acid over bimetallic PtCo alloys via the integration of theory and experiment. *ACS Catal.* **2024**, *14*, 18333–18344.

[17] Zhang, B. X.; Wang, J. M.; Liu, G. M.; Weiss, C. M.; Liu, D. Q.; Chen, Y. P.; Xia, L. X.; Zhou, P.; Gao, M. X.; Liu, Y. F. et al. A strongly coupled Ru–CrO_x cluster-cluster heterostructure for efficient alkaline hydrogen electrocatalysis. *Nat. Catal.* **2024**, *7*, 441–451.

[18] Wang, Z. L.; Li, S. R.; Zhang, G. F.; Yu, X.; Zhao, Z. Y.; Zhang, Y. P.; Shi, Y.; Zhu, H. B.; Xiao, X. C. Efficient electrocatalytic overall water splitting of porous 3D $CoPt_3$/a-FCWO-NS heterostructures: Morphology modulation and interfacial engineering for the formation of crystalline-amorphous nanosheets. *Appl. Catal. B: Environ.* **2024**, *342*, 123387.

[19] Yu, S. W.; Kwon, S.; Chen, Y. Z.; Xie, Z. H.; Lu, X. E.; He, K.; Hwang, S.; Chen, J. G.; Goddard III, W. A.; Zhang, S. Construction of a Pt–CeO_x interface for the electrocatalytic hydrogen evolution reaction. *Adv. Funct. Mater.* **2024**, *34*, 2402966.

[20] Wang, T. J.; Sun, L. B.; Ai, X.; Chen, P.; Chen, Y.; Wang, X. Boosting formate electrooxidation by heterostructured PtPd alloy and oxides nanowires. *Adv. Mater.* **2024**, *36*, 2403664.

[21] Xiong, H.; Du, C. F.; Ma, Z. L.; Zhi, R. C.; Hao, S. S.; Zhao, X. Y.; Liu, Z.; Xu, F.; Wang, H. Q. Rational design of multiple heterostructures with synergistic effect for efficient and stable hydrogen evolution toward industrial alkaline water splitting. *Adv. Funct. Mater.* **2024**, *34*, 2402298.

[22] Jiang, S. W.; Xue, J. W.; Liu, T.; Huang, H.; Xu, A. R.; Liu, D.; Luo, Q. Q.; Bao, J.; Liu, X. K.; Ding, T. et al. Visualization of the distance-dependent synergistic interaction in heterogeneous dual-site catalysis. *J. Am. Chem. Soc.* **2024**, *146*, 29084–29093.

[23] Shan, A. X.; Teng, X. A.; Zhang, Y.; Zhang, P. F.; Xu, Y. Y.; Liu, C. R.; Li, H.; Ye, H. Y.; Wang, R. M. Interfacial electronic structure modulation of Pt–MoS_2 heterostructure for enhancing electrocatalytic hydrogen evolution reaction. *Nano Energy* **2022**, *94*, 106913.

[24] Zhou, T. T.; Dong, K. Y.; Zheng, Z.; Yuan, Q. Coupling of alloying and interface effects in dendritic Au-doped PtPd alloy/dumbbell-like bismuth telluride heterostructures for ethanol and methanol electrooxidation. *Rare Met.* **2025**, *44*, 3119–3129.

[25] Wei, L. C.; Yan, W.; Huang, Z. L.; Li, R. C.; Kong, Q. Y.; Huang, W. H.; Pao, C. W.; Hu, Z. W.; Lin, H. X.; Chen, N. J. et al. Phase and interface engineering of a Ru–Sn nanocatalyst for enhanced alkaline hydrogen oxidation reaction. *Energy Environ. Sci.* **2024**, *17*, 5922–5930.

[26] van Deelen, T. W.; Hernández Mejía, C.; de Jong, K. P. Control of metal-support interactions in heterogeneous catalysts to enhance activity and selectivity. *Nat. Catal.* **2019**, *2*, 955–970.

[27] Li, C. Y.; Shi, Y. Y.; Zhang, Z. C.; Ni, J.; Wang, X. Y.; Lin, J. X.; Lin, B. Y.; Jiang, L. L. Improving the ammonia synthesis activity of Ru/CeO_2 through enhancement of the metal-support interaction. *J. Energy Chem.* **2021**, *60*, 403–409.

[28] He, M.; Ge, J.; Lin, Z. Q.; Feng, X. H.; Wang, X. W.; Lu, H. B.; Yang, Y. L.; Qiu, F. Thermopower enhancement in conducting polymer nanocomposites via carrier energy scattering at the organic-inorganic semiconductor interface. *Energy Environ. Sci.* **2012**, *5*, 8351–8358.

[29] Zhang, C. Y.; Peng, S. L.; Wei, Y. C.; Li, C. Y.; Han, J. Y.; Zhou, H. X.; Jiang, Y. D.; Wang, J. Photodetectors based on vertically stacked Bi_2Te_3/WSe_2 heterojunctions for visible to near-infrared photodetection. *ACS Appl. Nano Mater.* **2024**, *7*, 10565–10572.

[30] Liu, X. F.; Si, Y. B.; Li, K.; Xu, Y. N.; Zhao, Z. P.; Li, C. Q.; Fu, Y. Z.; Li, D. Exploring sodium storage mechanism of topological insulator Bi_2Te_3 nanosheets encapsulated in conductive polymer. *Energy Storage Mater.* **2021**, *41*, 255–263.

[31] Farber, E. M.; Seraphim, N. M.; Tamakuwala, K.; Stein, A.; Rücker, M.; Eisenberg, D. Porous materials: The next frontier in energy technologies. *Science* **2025**, *390*, eadn9391.

[32] Zhang, M. Y.; Zhu, W.; Liu, Z. Y.; Chen, S. R.; Zhou, D. Y.; Mu, X. Q.; Zhuang, Z. C.; Wang, S. C.; Yang, J. R.; Du, Y. P. et al. Selective

sieving effect of multi-atomic bismuth interfaces for efficient formate electrosynthesis and evolution at industrial current density. *Angew. Chem., Int. Ed.* **2025**, *64*, e202510206.
[33] Zhou, F. Y.; Ruan, Y. E.; Li, F.; Tian, L.; Zhu, M. Z.; Tie, W.; Tian, X. Y.; Wang, B.; Liu, P. G.; Xu, J. et al. Integrating single Ni site and PtNi alloy on two-dimensional porous carbon nanosheet for efficient catalysis in fuel cell. *Nano Res.* **2024**, *17*, 6916–6921.
[34] Zhao, H. Y.; Chen, D.; Dong, Y. X.; Chen, Y. R.; Jiao, J. X.; Yu, J.; Li, Y. W.; Mu, S. C. $RuTe_2$ heterophase homojunction induced built-in electric field drives ultrafast hydrogen evolution reaction kinetics. *Appl. Catal. B: Environ. Energy* **2025**, *374*, 125409.
[35] Zeng, X. J.; Nie, T. L.; Zhao, C.; Yu, R. H. Homogeneous–heterogeneous interfaces in 2D/2D $CoAl/Co_9S_8/Ni_3S_4$ heterostructures for electromagnetic wave absorption. *J. Colloid Interface Sci.* **2023**, *648*, 940–950.
[36] Li, Z. G.; Tian, W. J.; Hu, K. S.; Guo, Y. J.; Tian, X. T.; Kang, W. J.; Li, R.; Qu, K. G.; Wang, L.; Meng, F. P. et al. Oxygen-driven reconstruction activates quasi-single Pd sites in hollow PdAg nanotubes for zinc-air and fuel cells. *Adv. Sci.* **2025**, *12*, e09329.
[37] Liu, J. W.; Duan, R. H.; Xu, Y. F.; Zhang, C.; Lv, C. D.; Hu, E. H.; Gao, J. J.; Han, B.; Lee, C.; Liu, Z. et al. Decoupled control of CO_2 and nitrate reduction intermediates to enable efficient tandem urea electrosynthesis. *ACS Nano* **2025**, *19*, 29646–29656.
[38] Chang, Y.; Cheng, Y.; Feng, Y. L.; Li, K.; Jian, H.; Zhang, H. Y. Upshift of the d band center toward the fermi level for promoting silver ion release, bacteria inactivation, and wound healing of alloy silver nanoparticles. *ACS Appl. Mater. Interfaces* **2019**, *11*, 12224–12231.
[39] Yu, J.; Li, J.; Xu, C. Y.; Li, Q. Q.; Liu, Q.; Liu, J. Y.; Chen, R. R.; Zhu, J. H.; Wang, J. Modulating the d-band centers by coordination environment regulation of single-atom Ni on porous carbon fibers for overall water splitting. *Nano Energy* **2022**, *98*, 107266.
[40] Zhang, M. Y.; Luo, X.; Zhou, D. Y.; Wang, S. C.; Chen, S. R.; Du, Y. P.; Zhuang, Z. C.; Yang, J. R.; Zhu, W.; Liu, S. L. et al. Multiscale manipulation of functional imperfection atomic interfaces. *Acc. Chem. Res.* **2026**, *59*, 322–336.
[41] Du, Y. P.; Mu, X. Q.; Wang, S. C.; Zhang, Y. F.; Chen, F. J.; Zhang, M. Y.; Li, J. L.; Cao, P. P.; Yuan, J. Y.; Zhang, Y. et al. Atomically dispersed catalysts: For the efficient and stable industrial electrosynthesis of H_2O_2. *Energy Environ. Sci.* **2025**, *18*, 5833–5867.
[42] Lin, X.; Geng, S. Z.; Du, X. L.; Wang, F. T.; Zhang, X.; Xiao, F.; Xiao, Z. Y.; Wang, Y. C.; Cheng, J.; Zheng, Z. F. et al. Efficient direct formic acid electrocatalysis enabled by rare earth-doped platinum-tellurium heterostructures. *Nat. Commun.* **2025**, *16*, 147.
[43] Peng, Y.; Li, L. D.; Tao, R.; Tan, L. Y.; Qiu, M. N.; Guo, L. One-pot synthesis of Au@Pt star-like nanocrystals and their enhanced electrocatalytic performance for formic acid and ethanol oxidation. *Nano Res.* **2018**, *11*, 3222–3232.
[44] Liu, L. B.; Jin, L. J.; Xiao, Z. Y.; Fang, N.; Lin, X.; Ji, Y. J.; Wang, Y. C.; Li, Y. Y.; Huang, X. Q.; Bu, L. Z. Heterostructured Pt–PbS nanobelt achieves remarkable direct formic acid oxidation catalysis. *Nano Lett.* **2024**, *24*, 8162–8170.
[45] Li, S. M.; Zhang, J. Y.; Pei, S. Z.; Wu, K. J.; Zhao, B. W.; Wang, M.; Li, Y. W. Surface diffusion-limited dealloying: A strategy for porosity construction in small-sized alloy nanoparticle electrocatalysts. *Nano Res.* **2025**, *18*, 94907877.
[46] Dong, K. Y.; Yuan, Q. High-index facet-rich quaternary PtCuFeCo octopods as anti-CO poisoning bifunctional electrocatalysts for direct methanol/ethylene glycol fuel cells. *Chem. Sci.* **2025**, *16*, 9854–9862.
[47] Sun, Y. J.; Chen, W. B.; Zhang, W. S.; Nie, Y.; Zhang, Q. H.; Gu, L.; Luo, M. C.; Guo, S. J. Trimetallic porous PtIrBi nanoplates with robust CO tolerance for enhanced formic acid oxidation catalysis. *Adv. Funct. Mater.* **2023**, *33*, 2303299.
[48] Liu, D.; Xie, M. L.; Wang, C. M.; Liao, L. W.; Qiu, L.; Ma, J.; Huang, H.; Long, R.; Jiang, J.; Xiong, Y. J. Pd–Ag alloy hollow nanostructures with interatomic charge polarization for enhanced electrocatalytic formic acid oxidation. *Nano Res.* **2016**, *9*, 1590–1599.
[49] Weng, C. C.; Wang, C.; Song, Y.; Zhang, Y. X.; Zou, K.; Chen, H. W.; Yang, X.; Lin, W. *In-situ* reconstruction of active bismuth for enhanced CO_2 electroreduction to formate. *Chem. Eng. J.* **2025**, *505*, 159732.
[50] Ma, R. Z.; Zhang, J.; Gong, J. X.; Lin, Y. X.; Zhang, J. L.; Huang, Z. Q.; Chang, C. R.; Liu, S. J.; Zhu, W.; Wang, Y. X. et al. The cooperative effects of the Rh-M dual-metal atomic pairs in formic acid oxidation. *Angew. Chem., Int. Ed.* **2025**, *64*, e202503095.
[51] Zhao, F. L.; Nie, S. Y.; Wu, L.; Yuan, Q.; Wang, X. Porous, ultrathin PtAgBiTe nanosheets for direct hydrazine hydrate fuel cell devices. *Adv. Mater.* **2023**, *35*, 2303672.
[52] Joo, J.; Uchida, T.; Cuesta, A.; Koper, M. T. M.; Osawa, M. The effect of pH on the electrocatalytic oxidation of formic acid/formate on platinum: A mechanistic study by surface-enhanced infrared spectroscopy coupled with cyclic voltammetry. *Electrochim. Acta* **2014**, *129*, 127–136.
[53] Cui, C. H.; Li, H. H.; Cong, H. P.; Yu, S. H.; Tao, F. Direct evidence for active site-dependent formic acid electro-oxidation by topmost-surface atomic redistribution in a ternary PtPdCu electrocatalyst. *Chem. Commun.* **2012**, *48*, 12062–12064.
[54] Liang, M. C.; Xia, T. Y.; Gao, H.; Zhao, K.; Cao, T. Q.; Deng, M.; Ren, X. Y.; Li, S. F.; Guo, H. Z.; Wang, R. M. Modulating reaction pathways of formic acid oxidation for optimized electrocatalytic performance of PtAu/CoNC. *Nano Res.* **2022**, *15*, 1221–1229.
[55] Liu, Z. J.; Wang, Z. Y.; Wang, Z. Y.; Yuan, H.; Bai, Y. K.; Wang, X. X.; Mu, Z. R.; Wu, C. X.; Liu, K.; Hu, Z. et al. Lattice-mismatch-induced formation of defect-rich Pd–Cu alloy nanocages for enhanced formic acid oxidation activity. *Sci. China Chem.* **2025**, *68*, 481–491.
[56] Zheng, J. H.; Zhang, J. L.; Li, G.; Zhang, J. M.; Zhang, B. W.; Jiang, Y. X.; Sun, S. G. Tuning atomic Pt site surface on PtAu alloy toward electro-oxidation of formic acid. *Mater. Today Energy* **2022**, *27*, 101028.
[57] Wang, Y. F.; Zhang, S. L.; Deng, Y. X.; Luan, S. H.; Wang, C. K.; Ding, L. F.; Jiang, X.; Sun, D. M.; Tang, Y. W. PtPdAg nanotrees with low Pt content for high CO tolerance within formic acid and methanol electrooxidation. *Rare Met.* **2025**, *44*, 300–310.
[58] Sun, Y. Y.; Polani, S.; Luo, F.; Ott, S.; Strasser, P.; Dionigi, F. Advancements in cathode catalyst and cathode layer design for proton exchange membrane fuel cells. *Nat. Commun.* **2021**, *12*, 5984.
[59] Ahn, C. Y.; Park, J. E.; Kim, S.; Kim, O. H.; Hwang, W.; Her, M.; Kang, S. Y.; Park, S.; Kwon, O. J.; Park, H. S. et al. Differences in the electrochemical performance of Pt-based catalysts used for polymer electrolyte membrane fuel cells in liquid half- and full-cells. *Chem. Rev.* **2021**, *121*, 15075–15140.
[60] Wang, L. P.; Yu, Z. Y.; Yan, W.; Liu, L. B.; Wang, M. J.; Kong, Q. Y.; Hu, Z. W.; Geng, H. B.; Huang, X. Q.; Li, Y. H. Palladium chalcogenide nanosheets with p–d orbital hybridization for enhanced alcohol electro-oxidation performance. *Appl. Catal. B: Environ.* **2024**, *343*, 123564.
[61] Huang, Z. L.; Hu, S. N.; Sun, M. Z.; Xu, Y.; Liu, S. H.; Ren, R. J.; Zhuang, L.; Chan, T. S.; Hu, Z. W.; Ding, T. Y. et al. Implanting oxophilic metal in PtRu nanowires for hydrogen oxidation catalysis. *Nat. Commun.* **2024**, *15*, 1097.